A RADIOMETRIC CONSISTENT RENDER PROCEDURE FOR PLANETS AND MOONS

Andrea Pizzetti[1*], Paolo Panicucci[1] and Francesco Topputo[1]

[1]Politecnico di Milano, Department of Aerospace Science and Technology, Via La Masa 34, Milan, 20156, Italy

[*][andrea.pizzetti@polimi.it]

Abstract. *This paper outlines the development and capabilities of a radiometric-consistent render to image at any observer pose a resolved spherical object and to compute pixel-wise spectral radiometric quantities within any user-defined waveband. Several reflection models are available and albedo, displacement and normal maps can be included to ensure radiometric fidelity. The tool is validated against real images of the Moon taken by the AMIE camera on-board of SMART-1 mission.*

Introduction. The effectiveness of GNC vision-based algorithms strongly relies on the physical consistency of the models and data used for their validation. At the same time, a strong push is present nowadays toward the use of data-driven algorithms which rely on vast amounts of diverse and high-quality data to grant generalization and performance. However, this is in conflict with the issue of data scarcity that characterizes the space domain. The current state-of-the-art approaches exploit synthetic data generated through render engines. Although common open-source render engines are useful for generating huge amount of data, they often suffer from physical inconsistencies and do not grant full control over physical phenomena and parameters to the user, limiting their degree of radiometric realism.

The solution proposed in this paper allows to generate renderings of spherical bodies with radiometric consistency and can be used either as starting point for a tailored high-fidelity render engine for space imaging applications or as a design tool for radiometric analysis of resolved spherical objects.

Model Overview. Consider the spherical body shown in Figure 1, where the point C is centered on an infinitesimal surface cap S_C and δ_I and δ_R are the angle of incidence and reflection of the light at C. The spectral power reflected by the cap and collected by the camera is given by Equation 1.

$$P_\lambda = \Omega \cdot I_\lambda = F_\lambda \cdot \underbrace{\Omega \int_{S_C} f_r(\delta_I, \delta_R) \cos \delta_I dS}_{PF} \qquad (1)$$

Where Ω is the spherical angle subdued to the pupil area at the cap-camera distance, I_λ is the reflected spectral intensity and f_r is the Bi-directional Reflectance Distribution Function (BRDF). The core of the model is the computation of a point cloud of $\mathcal{PF}_i$ coefficients representing the ratio of the power P collected from each surface S_i over the radiant flux density F that arrives parallel to the body. Assuming spectral independence of the

BRDF, the computational load is reduced as this coefficient is the same for every wavelength λ.

Taking inspiration from the approach employed in [1], $\mathcal{PF}_i$ is computed analytically as function of the phase angle α, parametrizing the BRDF to the longitude ϕ and latitude θ angles referred to the XYZ frame shown in Figure 1. While in [1] the integral is computed altogether for the full sphere, however, here each discretized surface cap is considered separately to obtain the point cloud.

$$\mathcal{PF}_i(\alpha) = \Omega R^2 \int_{\Delta\phi_i} \int_{\Delta\theta_i} f_r(\theta, \phi) \sin^3 \theta \cos(\phi) \cos(\alpha - \phi) d\theta d\phi$$
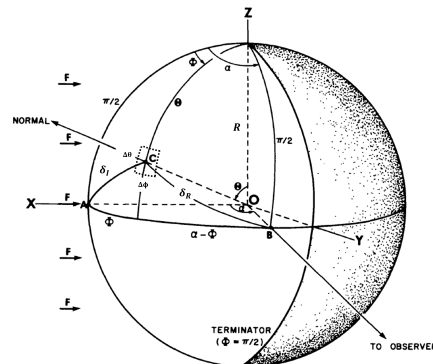
Figure 1. Radiometric model framework (modified from [1])

The BRDF is scaled by a constant γ which embeds the Bond albedo coefficient p. For instance, for a Lambertian reflection model $f_r = \gamma$ with $\gamma = \frac{p}{\pi}$ and for an Area reflection model $f_r = \gamma \sec(\delta_I)$ with $\gamma = \frac{p}{2\pi}$. Note that the albedo map can be included considering a local albedo p_i interpolated at each longitude and latitude. The same can be done for the displacement map and the normal map, correcting the local radius R_i and the local incidence and reflection angles δ_{I_i} and δ_{R_i}.

The overall procedure is shown in Figure 3. For every point $i = 1, \ldots, N$, its position $\vec{r}_i$ and value $\mathcal{PF}_i$ are computed. Note that points falling outside the Field Of View (FOV) of the camera are skipped for computational efficiency purposes. Then, the 3D point cloud is projected into the image plane and the values are binned through a gridding method to obtain a 2D matrix PF of interval-valued points, each interval representing a single pixel. Note that projection artifacts and aliasing might be present due to the proposed approach. Two main countermeasures were introduced to mitigate this issue:

- A *non-uniform sampling* for the longitude/latitude discretization intervals, such that the projection of the sampled points on the camera frame is instead spread uniformly.
- An *area-weighted gridding* to split the value $\mathcal{PF}_i$ of each point to the closest pixels according to the percentage of the surface S_i that, once projected into the image plane, falls into each neighboring pixel.

Once the PF matrix is available, Equation 1 is applied to obtain the spectral power collected by each pixel and consequently the spectral photon count rate by dividing for the photon energy hc/λ. By then applying the transmissivity T and quantum efficiency QE scaling, the spectral electron count rate is obtained. Finally, the digitalized image is obtained performing integration across the desired waveband, multiplication for the exposure time and Full-Well Capacity (FWC) quantization. These operations are shown in Equation 2.

$$\text{IMG} = \frac{2^{N_{bit}} - 1}{\text{FWC}} \, \Delta t_{exp} \int_{\Delta\lambda} QE_\lambda \, T_\lambda \, \frac{\lambda}{hc} \, P_\lambda d\lambda \quad (2)$$

The capabilities of the model are shown in Figure 4 and Figure 5 using a $f/2.5$ camera with FOV $= 6°$. The detector has a resolution of 1024 px with pixel size of 13.3 μm and FWC $= 10^5 \, e^-$. The 450-820 nm waveband is used with QE and T assumed constant and unitary. As it can be seen, bodies can be rendered offset from the optical axis, with any user-provided albedo texture and at different poses and lighting conditions with no shortcomings.

Validation. The model is validated using real space imagery of the Moon taken by the AMIE camera on-board of the SMART-1 mission [2]. The image database[1] includes hundreds of pictures acquired at different poses and is deemed applicable for validation as the images are labeled with exposure time metadata and SPICE kernels are available. The position and orientation of the AMIE camera is extracted using SPICE routines and plugged into the analytical model. An Oren-Nayar reflection model [3] is assumed for the Moon, with a Bond albedo $p = 0.15$ and a roughness $\rho = 0.3$. An example of comparison for an image[2] taken at 30 ms is shown in Figure 2.

A quantitative assessment is also performed using Structural Similarity Index Measure (SSIM) [4] after alignment of the images through normalized cross-correlation and removal of background noise from the AMIE image, which was not modelled for in the radiometric model. Even if differences were expected due to uncertainties in the pose [5], camera alignment and reflection model parameters, a good match is observed for all the three factors, as depicted in Figure 6. The absence of shadows and diffraction/distortion effects in the model can explain the small differences observable in the structure metric. Following this analysis, the tool can be considered validated at least on a first order of magnitude.

---

[1] SMART-1 AMIE archive
[2] AMI_EE3_040819_00208_00030.IMG

(a) AMIE   *(b) Render*

Figure 2. Model validation

Conclusions. At the current stage, the model proved to be useful for the preliminary sizing of cameras and the design of optical navigation algorithms. For instance, from the electron count rate the optimal camera exposure time bounds can be selected depending on the target body and the information that needs to be extracted from the image. Moreover, the tool is also deemed necessary to perform tests in an optical facility, where the knowledge of screen excitance is mandatory to correctly stimulate the sensor in terms of collected energy.

Suggested future works concern development efforts to increase the fidelity of the render. In particular, the following features are identified as useful additions:

- Shadow map to model occlusions.
- Modelling of atmosphere and clouds.
- Addition of camera/detector errors and noises.
- More complex reflection models such as Hapke [6], where the BRDF has spectral variability.

The afore-mentioned upgrades would increase the representativeness especially at short distances, where the impact of local features is no longer negligible. For what concern mid-to-far ranges, the proposed rendering procedure is instead deemed reliable for many scenarios of interest, such as optical navigation experiments.

References.

[1] T. P. Lester, M. L. McCall, and J. Tatum, "Theory of planetary photometry," *Journal of the Royal Astronomical Society of Canada, vol. 73, Oct. 1979, p. 233-257.*, vol. 73, pp. 233–257, 1979.

[2] B. Grieger, "The calibration of amie images," tech. rep., ESA technical note S1-AMIE-SGSTN-013, 2008.

[3] M. Oren and S. K. Nayar, "Generalization of lambert's reflectance model," *Proceedings of the 21st annual conference on Computer graphics and interactive techniques*, 1994.

[4] Z. Wang, A. Bovik, H. Sheikh, and E. Simoncelli, "Image quality assessment: from error visibility to structural similarity," *IEEE Transactions on Image Processing*, vol. 13, no. 4, pp. 600–612, 2004.

[5] I. Belgacem, G. Jonniaux, and F. Schmidt, "Image processing for precise geometry determination," *Planetary and Space Science*, vol. 193, p. 105081, 2020.

[6] B. Hapke, "Bidirectional reflectance spectroscopy: 1. theory," *Journal of Geophysical Research: Solid Earth*, vol. 86, no. B4, pp. 3039–3054, 1981.
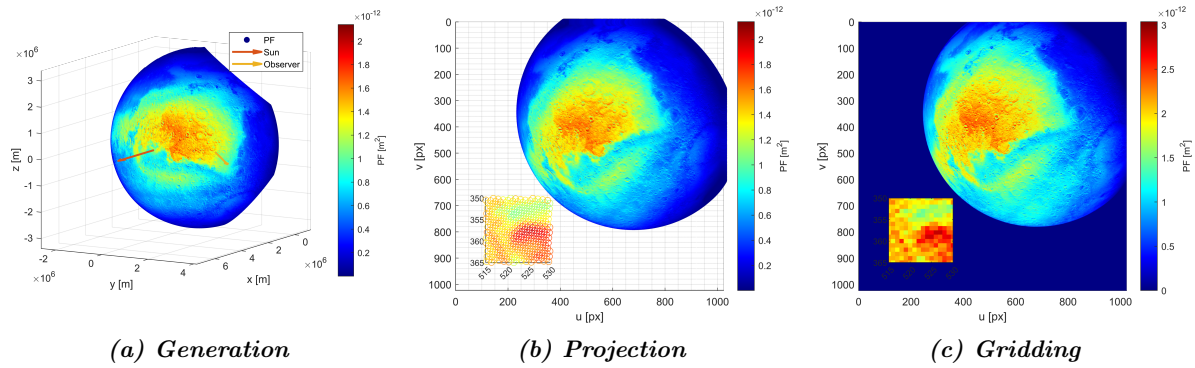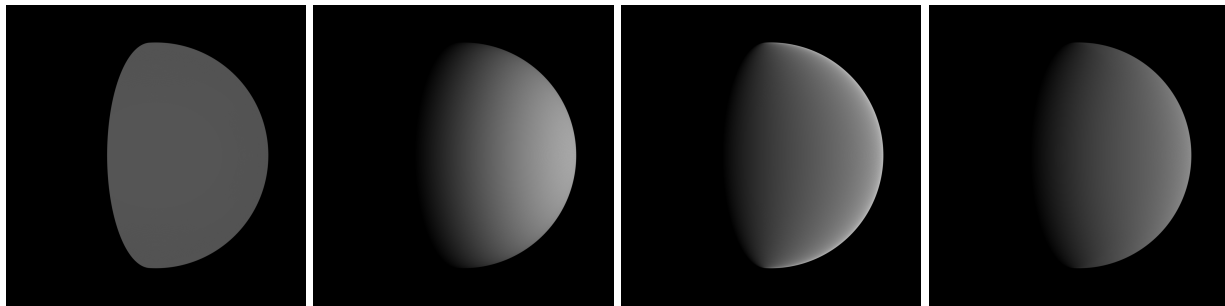
(a) Generation   (b) Projection   (c) Gridding

Figure 3. Visualization of the operations applied on the point cloud of $\mathcal{PF}_i$ coefficients

(a) Area   (b) Lambert   (c) Lommel-Seeliger   (d) Oren-Nayar

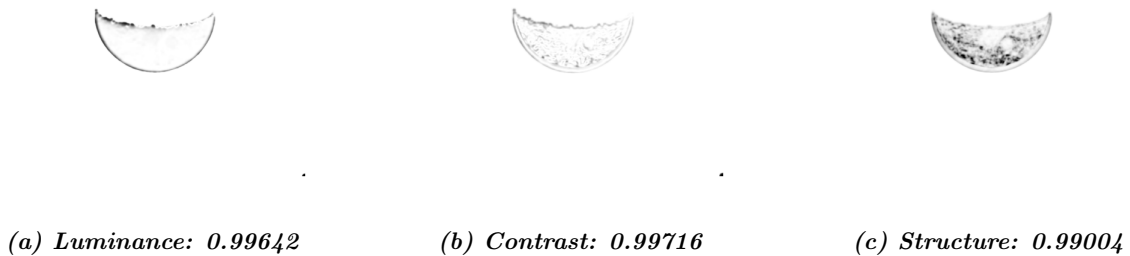*Figure 4. Comparison of reflection models for a texture-less sphere*

(a) Mars, $\alpha = 0°$ (b) Mars, $\alpha = 40°$ (c) Moon, $\alpha = 80°$ (d) Moon, $\alpha = 120°$

Figure 5. Renderings at different viewing and illumination conditions with a Lambert reflection model

(a) Luminance: 0.99642   (b) Contrast: 0.99716   (c) Structure: 0.99004

Figure 6. Similarity assessment of the validation image using SSIM